

SCIENTIFIC REPORTS



OPEN

Experimentally validated full-vectorial model of wavelength multicasting via four-wave mixing in straight waveguides

Kai Guo^{1,2,3}, Jiacheng Feng¹, Xiaodong Shi², Jiehui Li⁴, Minghong Gao⁵, Hui Jing², Xiaolin Wang¹, Junbo Yang³ & Haiyan Ou²

We derive full-vectorial nonlinear propagation equations of dual-pumped four-wave mixing in straight waveguides, which are valid in characterizing the one-to-six wavelength multicasting. Special attention is paid to the resulting idler wavelengths and their conversion efficiency, which enables the optimization of the experimental designs, including the incident wavelength and the power of pumps and signal. We validate the model by comparing the numerical simulation to the experimental measurement in a silicon-on-insulator waveguide, for the first time to our best knowledge, and achieve a good agreement. We further derive the general form of the proposed model for the case of using multiple pumps, which holds a potential to numerically predict the performance of complex wavelength multicasting, and essentially guide the waveguide designs.

Four-wave mixing (FWM), a third-order nonlinear optical effect, makes possible a number of key features for all-optical signal processing¹. Specifically, two pump photons (subscripted as p and q) annihilate and generate a pair of signal-idler photons (subscripted as s and i), in which the angular frequencies follow the energy conservation $\omega_s + \omega_i = \omega_p + \omega_q$. FWM facilitates the energy conversion from one wavelength to another, known as the wavelength conversion², or to several wavelengths, known as the wavelength multicasting³, which are of great significance in the wavelength division multiplexing networks, as the data packet is converted simultaneously⁴. While the initial experiments of FWM were carried out in highly nonlinear optical fibers^{2,3}, the integrated platforms especially the silicon-on-insulator (SOI) waveguides, recently attract more research interest. SOI waveguides are compatible with the complementary metal-oxide semiconductor technology, which enables compact integration of opto-electronic components for building the on-chip optical communication system⁵. Moreover, SOI waveguides facilitate high refractive index contrast between the core and the cladding that ensures strong nonlinear interaction and tailorable group-velocity dispersion profile⁶ that benefits the phase matching⁷. Therefore, efficient wavelength conversion^{8–13} and wavelength multicasting^{14–21} have been demonstrated in a variety of waveguide designs, which takes the merits of broadband operation compared to that demonstrated in atomic or atomic-like mediums^{22–24}.

However, few of the wavelength multicasting demonstrations pay attention to the numerical analysis. Previous studies²⁵ have presented the nonlinear propagation equations in straight waveguides, yet by using the optical intensity with respect to the effective mode area, it remains difficult to directly compare the numerical simulations to the experimental measurements of the optical power. On the other hand, the theoretical models for optical fibers^{26–28}, in which the scalar-approach is often assumed²⁹, are invalid for straight waveguides because of the relatively large refractive index contrast. Although a good agreement can be achieved by fitting the parameters in the scalar-approach model, the numerical predictions may lead to mistakes when evaluating the nonlinear refractive

¹College of Advanced Interdisciplinary Studies, National University of Defense Technology, Changsha, 410073, China. ²Department of Photonics Engineering, Technical University of Denmark, Kgs. Lyngby, 2800, Denmark. ³Center of Material Science, National University of Defense Technology, Changsha, 410073, China. ⁴Shanghai Institute for Advanced Communication and Data Science, Key Laboratory of Information Science of Electromagnetic Waves, Fudan University, Shanghai, 200433, China. ⁵College of Artificial Intelligence, National University of Defense Technology, Changsha, 410073, China. Correspondence and requests for materials should be addressed to K.G. (email: guokai07203@hotmail.com)

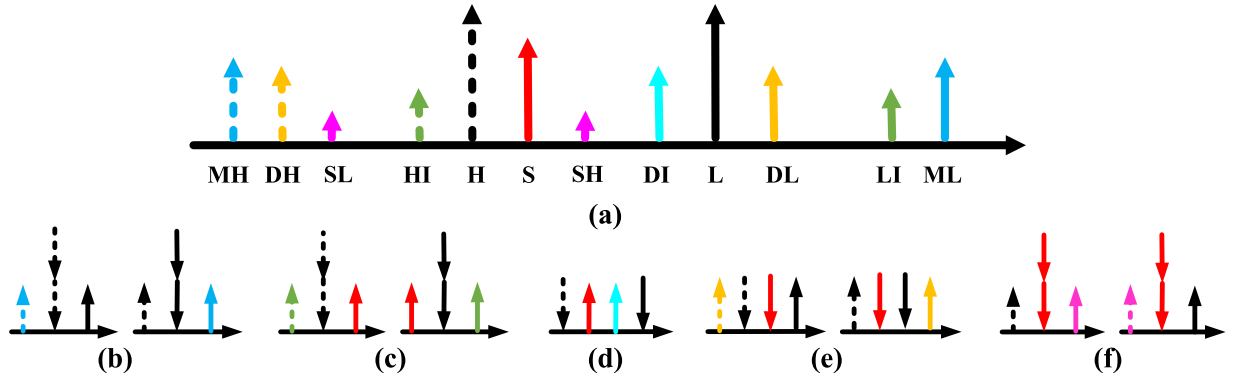


Figure 1. The output wavelengths and the corresponding energy conversion.

index and optimizing designs of new waveguides. Hence, a full-vectorial model is of great importance, which facilitates a solid theoretical understanding, takes a simple form and can be easily validated by experiments.

In this paper, we derive the full-vectorial nonlinear propagation equations for dual-pumped FWM processes. We predict the idler wavelengths through the energy conservation and characterize the conversion efficiency of the one-to-six wavelength multicasting configuration. We validate the model by comparing the numerical simulations to the experimental measurements in a SOI waveguide sample and further give the general form of the model in the cases of using multiple pumps.

Results

Numerical model. The electric and magnetic fields are expanded in a set of continuous wave (CW) frequency components, ω_n ,

$$\begin{cases} \mathbf{E}(\mathbf{r}, t) \\ \mathbf{H}(\mathbf{r}, t) \end{cases} = \frac{1}{2} \sum_n \frac{A_n(z)}{N_n} \begin{cases} \mathbf{F}(x, y) \\ \mathbf{U}(x, y) \end{cases} \exp(-i\omega_n t + i\beta_n z) + c. c., \quad (1)$$

where $\mathbf{r} = \{x, y, z\}$ denotes the position coordinate, A_n denotes the common amplitude varying along the longitudinal direction z , \mathbf{F}_n and \mathbf{U}_n denote the field distribution functions of the electric and magnetic field in the transverse dimension, respectively, β_n denotes the propagation constant and c. c. denotes the complex conjugate. To ensure that $|A_n|^2$ equals the optical power P_n in watts, the normalization factor N_n is given by³⁰

$$N_n^2 = \frac{1}{4} \int_{x,y} [\mathbf{F}_n \times \mathbf{U}_n^* + \mathbf{F}_n^* \times \mathbf{U}_n] \cdot \mathbf{z} \, dx dy, \quad (2)$$

where \mathbf{z} denotes the unit vector of the longitudinal direction. N_n can take a simpler form

$$N_n^2 = \frac{c}{2n_g} \int_{x,y} n_w^2(x, y) |\mathbf{F}_n|^2 \, dx dy, \quad (3)$$

where n_g and $n_w(x, y)$ are the group index and the transverse refractive index distribution of the waveguide, respectively³¹. By substituting Eq. (1) into Maxwell's equations, the propagation equation of the field amplitude at ω_n becomes³²⁻³⁴

$$\partial_z A_n(z) = \frac{i\omega_n}{4N_n} \int_S \mathbf{F}_n^* \cdot \mathbf{P}_n^{NL}(\mathbf{r}) \, ds, \quad (4)$$

where ∂_z denotes the differentiation of z . Assuming that the electronic response is instantaneous, the Kerr-induced nonlinear polarization can be expanded with different frequency components,

$$\mathbf{P}^{NL}(\mathbf{r}, t) = \frac{1}{2} \sum_n \mathbf{P}_n^{NL}(\mathbf{r}) \exp(-i\omega_n t + i\beta_n z) + c. c. \quad (5)$$

It can also be written as the tensor product

$$\mathbf{P}^{NL} = \varepsilon_0 \chi^{(3)} : \mathbf{E} \mathbf{E} \mathbf{E}, \quad (6)$$

where the third-order susceptibility tensor $\chi^{(3)}$ is assumed to be independent of frequency in the bandwidth of phase matching.

In the simple configuration we concerned, two pumps, subscripted as H (high frequency) and L (low frequency) and a signal, subscripted as S , are incident lights in the waveguide. The output wavelengths shown in Fig. 1 come from several FWM processes, which can be classified into the degenerate type pumped with the same frequency and the non-degenerate type pumped with different frequencies. Note that the incident wavelengths

may behave as either the pump or the signal of FWM, but only the energy conversion involving S can be used for wavelength multicasting. Specifically, the degenerate FWM pumped at H generate the idler wavelengths of MH and HI , when the signal is at L and S , respectively. Similar processes pumped at L generate the idler wavelengths of ML and LI . Moreover, the non-degenerate FWM, using two of the incident lights as the pumps and the third one as the signal, generates the idler wavelengths of DI , DH and DL . Additionally, when the incident power of S is comparable to that of H and L , efficient degenerate FWM pumped at S may take place, that H and L as the signal generate the idler SH and SL , respectively.

Typically, all frequency components are in the same polarization state and within the bandwidth of phase matching, thus, the electric field distribution function \mathbf{F} and the normalization factor N can be assumed to be frequency independent. Moreover, the spontaneous/cascaded/idler-induced processes bring negligible contributions to the output power at different wavelengths. To simplify the following descriptions particularly for the wavelength multicasting configuration, these terms are not concerned. Hence, assuming only $\chi_0^{(3)} = \chi_{iii}^{(3)}$ for $i = x$ or $i = y$ is nonzero, the nonlinearity induced polarization at H becomes

$$\mathbf{P}_h^{NL} = (|A_h|^2 + 2|A_l|^2 + 2|A_s|^2) A_h \frac{\epsilon_0}{4N^3} \chi_0^{(3)} (2|\mathbf{F}|^2 \mathbf{F} + (\mathbf{F} \cdot \mathbf{F}) \mathbf{F}^*), \quad (7)$$

and by inserting Eq. (7) into Eq. (4), the propagation equation of H becomes

$$\partial_z A_h = i\gamma_e (|A_h|^2 + 2|A_l|^2 + 2|A_s|^2) A_h, \quad (8)$$

where the complex nonlinear coefficient is given by

$$\gamma_e = \frac{\omega \epsilon_0 n_g^2 \int_{x,y} \chi_0^{(3)} \mathbf{F}^* \cdot [2|\mathbf{F}|^2 \mathbf{F} + (\mathbf{F} \cdot \mathbf{F}) \mathbf{F}^*] dx dy}{4c^2 \left(\int_{x,y} n_w^2 |\mathbf{F}|^2 dx dy \right)^2}. \quad (9)$$

To have a convenient form known from optical fibers²⁹, by only taking the nonlinear contribution of the core (footnoted by c) into account, the complex nonlinear coefficient can be written as

$$\gamma_e = \frac{\omega n_2}{c A_{\text{eff}}} + i \frac{\beta_T}{2 A_{\text{eff}}}, \quad (10)$$

where the nonlinear refractive index and the two-photon absorption coefficient are identified as

$$n_2 = \frac{3 \text{Re}(\chi_c^{(3)})}{4 n_c^2 \epsilon_0 c}, \quad \beta_T = \frac{3 \omega \text{Im}(\chi_c^{(3)})}{2 n_c^2 \epsilon_0 c^2}. \quad (11)$$

In crystalline-semiconductor waveguides, the polarization coefficient ζ_e needs to be included in Eq. (11), which describes the nonlinear response with the polarization state. Finally, the resulting effective mode area, which is the key point of the full-vectorial model, is given by

$$A_{\text{eff}} = \frac{3}{n_g^2 n_c^2 \int_c \mathbf{F}^* \cdot [2|\mathbf{F}|^2 \mathbf{F} + (\mathbf{F} \cdot \mathbf{F}) \mathbf{F}^*] dx dy} \left(\int_{x,y} n_w^2 |\mathbf{F}|^2 dx dy \right)^2. \quad (12)$$

To account for loss mechanisms in straight waveguides, it is necessary to introduce the loss term in nonlinear propagation equations. Specifically in SOI waveguides, the wavelength-independent linear loss α_l and the wavelength-dependent free-carrier absorption^{35,36} are included in the loss coefficient given by

$$\alpha_n = \alpha_l + 6 \times 10^{-10} \cdot \frac{\lambda_n^2 \tau \beta_T \sum_n |A_n|^4}{\hbar \omega A_{\text{eff}}^2}, \quad (13)$$

where τ denotes the free carrier lifetime. At this point, the nonlinear propagation equation at H becomes

$$\partial_z A_h = -\frac{1}{2} \alpha_h A_h + i\gamma_e (|A_h|^2 + 2|A_l|^2 + 2|A_s|^2) A_h, \quad (14)$$

which can be transferred to that at L and S by swapping the footnote “h” with “l” and “s”, respectively. Moreover, at the degenerate FWM induced idler wavelengths such as HI , the nonlinear propagation equations need to involve the phase matching term as

$$\partial_z A_{hi} = -\frac{1}{2} \alpha_{hi} A_{hi} + i\gamma_e (2|A_h|^2 + 2|A_l|^2 + 2|A_s|^2) A_{hi} + i\gamma_e A_h^2 A_s^* \exp[i(2\beta_h - \beta_s - \beta_{hi})z], \quad (15)$$

which can be transferred to that at LI by swapping the footnotes “hi” and “h” with “li” and “l”, respectively. Similarly, the nonlinear propagation equations at the non-degenerate FWM induced idler wavelengths such as DI is given by

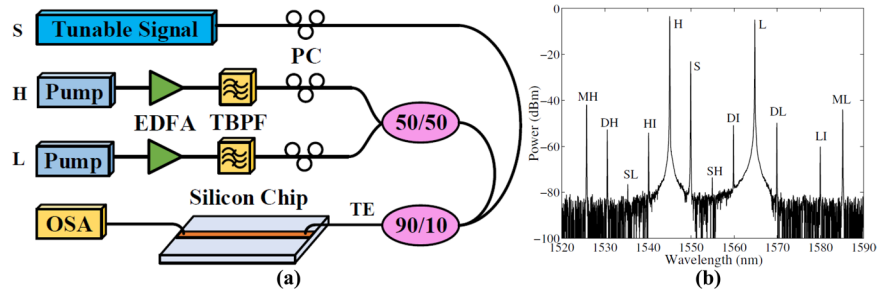


Figure 2. (a) A schematic of the validating experimental set up. EDFA: Erbium-doped fiber amplifier; TBPF: Tunable band-pass filter; PC: Polarization controller; OSA: Optical spectrum analyser. (b) The output spectrum when *H*, *L* and *S* are at 1545 nm, 1565 nm and 1550 nm, respectively.

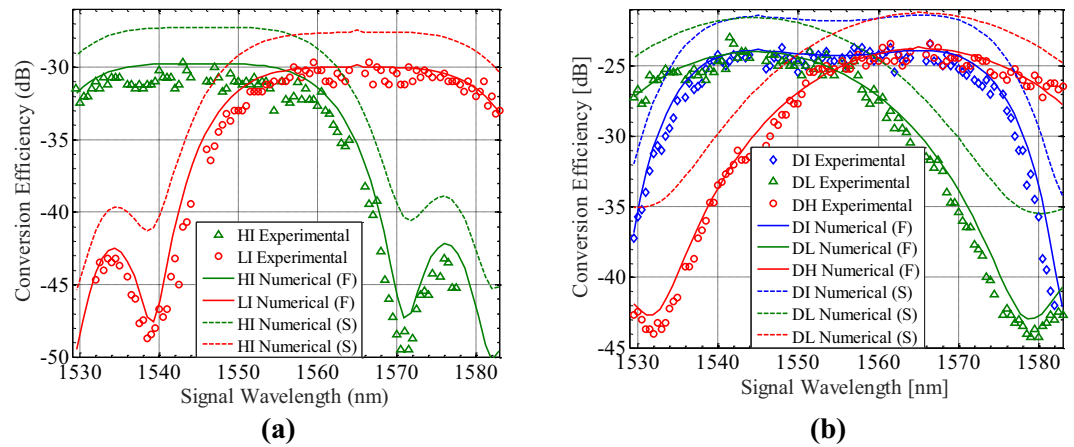


Figure 3. Full-vectorial numerical simulations (solid), Scalar-approach numerical simulations (dashed) and experimental measurements of the conversion efficiency at (a) *HI* (green triangles), *LI* (red circles), (b) *DI* (blue diamond), *DL* (green triangles) and *DH* (red circles). The incident power of pumps (1545 nm and 1565 nm) and signal are 10 dBm and -10 dBm, respectively.

$$\partial_z A_{di} = -\frac{1}{2}\alpha_{di}A_{di} + i\gamma_e(2|A_h|^2 + 2|A_l|^2 + 2|A_s|^2)A_{di} + i\gamma_e 2A_h A_l A_s^* \times \exp[i(\beta_h + \beta_l - \beta_s - \beta_{di})z], \tag{16}$$

which can be transferred to that at *DH* or *DL*, by swapping the footnotes “di” and “s” with “dh” and “l” or with “dl” and “h”, respectively. As the data packet at *S* is efficiently converted into packets at five idler wavelengths (omitting *SL* and *SH*), which forms a one-to-six wavelength multicasting configuration, Eq. (14–16) and their equivalents, constituting the full-vectorial model, make possible the numerical predictions of the experimental results.

Experimental validation. We validate the derived full-vectorial model by comparing the numerical simulations of the conversion efficiency, given by the ratio of idler to signal power at the waveguide output, to the experimental measurements in a SOI sample. In the simulation, the nonlinear refractive index n_2 is $6 \times 10^{-18} \text{ m}^2/\text{W}$, the two-photon absorption coefficient β_T is $4.5 \times 10^{-12} \text{ m/W}$, the free carrier lifetime is 10 ns and the polarization coefficient ζ_e is 1.25 for the transverse electric (TE) mode³⁷. The electric field profile is simulated through a finite difference mode solver³⁸ and the resulting effective mode area at 1550 nm is estimated as $0.06 \mu\text{m}^2$. Figure 2(a) shows the schematic of the validating experimental set up. Two pumps were power amplified by erbium-doped fiber amplifiers (EDFAs), where the incident amplified spontaneous emission was suppressed by tunable band-pass filters (TBPFs). The pumps were combined by a 50–50% coupler, followed by a 90–10% coupling with the tunable signal and were coupled in and out of the 1 cm waveguide sample through a pair of photonic crystal grating couplers (PCGCs)³⁹. Polarization controllers (PCs) were used to control the polarization state, so that the coupling loss of PCGCs, which are designed for TE mode, reached the minimum (5 dB per facet). Finally, the output spectrum was measured by an optical spectrum analyser (OSA), shown in Fig. 2(b), where the generated wavelengths agree well with predictions.

We firstly set the pumps at 1545 nm and 1565 nm with the same in-waveguide incident power of 10 dBm. We simulate the conversion efficiency versus the signal wavelength using two effective mode area definitions and compare them to the experimental measurements with an incident signal power of -10 dBm. The experimental data, of which the idler power reaches the background noise level of the OSA, is omitted. Figure 3(a) shows that

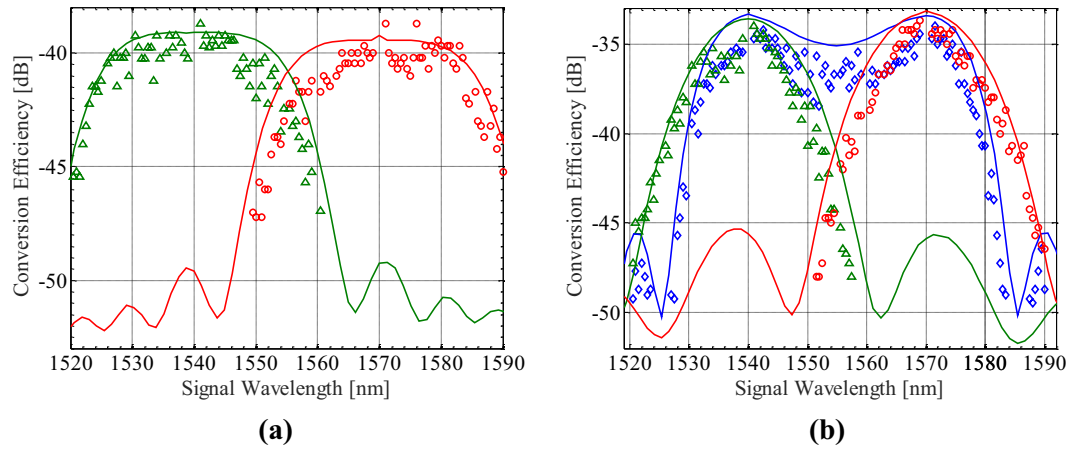


Figure 4. Numerical simulations (solid) and experimental measurements of the conversion efficiency at (a) *HI* (green triangles), *LI* (red circles), (b) *DI* (blue diamond), *DL* (green triangles) and *DH* (red circles). The incident power of pumps (1540 nm and 1570 nm) and signal are 5 dBm and -10 dBm, respectively.

for the degenerate FWM induced idlers, *HI* and *LI*, the maximal conversion efficiency of -30 dB takes place when the wavelength of *S* approaches to that of *H* and *L*, respectively. Since the linear phase mismatch corresponding to the propagation constant difference of four waves in Eq. (15) remains negative, the conversion efficiency versus signal wavelength behaves top-flattened with a 1 dB bandwidth of 24 nm. Figure 3(b) shows that for the non-degenerate FWM induced idlers, the maximal conversion efficiency reaches -24 dB, due to the factor of 2 in the final term of Eq. (16) rather than the factor of 1 in the final term of Eq. (15). For *DL* and *DI*, such a maximum takes place when the wavelength of *S* approaches to that of *H*, while for *DH* and *DI*, such a maximum takes place when the wavelength of *S* approaches to that of *L*. The 1 dB bandwidth for *DI* reaches 34 nm, however for *DH* and *DL*, it reduces to only 16 nm because of the relatively larger linear phase mismatch depending on the pump detuning. Note that the effective mode area is estimated as $0.06 \mu\text{m}^2$ and $0.04 \mu\text{m}^2$, by using the full-vectorial definition and the scalar-approach definition, respectively. As can be seen, the full-vectorial simulations (solid) fit well with the experimental results, while the conversion efficiency predicted by the scalar-approach simulations (dashed) are about 3 dB higher. Such a comparison validates the accuracy of the proposed full-vectorial model, in addition to strengthening the results presented in the previous study³⁴.

We then set the pumps at 1540 nm and 1570 nm, meanwhile reduce the incident power down to 5 dBm. Figure 4(a) shows that for the degenerate FWM induced idlers, the maximal conversion efficiency reduces to -38 dB, but the 1 dB bandwidth remains unchanged, which reveals the fact that high incident pump power enables high conversion efficiency. Figure 4(b) shows that for the non-degenerate FWM induced idlers, the maximal conversion efficiency reduces to -33 dB. Although the pump detuning of 30 nm enables more separable idler wavelengths, the 1 dB bandwidth reduces to 24 nm for *DI* and 12 nm for *DH* and *DL*. The experimental measurements also agree well with the numerical simulations, except for some small disagreement from the alignment drift, the incident power fluctuation and especially the unfiltered amplified spontaneous emission, which becomes more apparent by turning down the amplified power of EDFAs⁴⁰.

Being experimentally validated, the proposed full-vectorial model makes possible the optimization of the experimental designs. The conversion efficiency becomes higher by turning up the incident pump power, but remains unchanged by turning up the incident signal power. The increase of the pump detuning may result in the reduction of the bandwidth that corresponds to efficient wavelength conversion. To achieve high conversion efficiency for all idlers, the signal wavelength needs to approach to but not equal to the central wavelength of the two pumps. Additionally, to broaden the bandwidth especially for the non-degenerate FWM induced idlers, the waveguide designs that enable near-zero anomalous group-velocity dispersion at concerned wavelengths are desired.

General model for multiple-pumped wavelength multicasting. We derive the general form of the full-vectorial model for more complicated wavelength multicasting configuration using multiple pumps. Assume that N pumps and one signal are incident in the waveguide, where the initial power at all wavelengths are the same. The nonlinear propagation equation at one of the incident pumps, of which the amplitude is denoted by A_p for $p = 1, 2, \dots, N$, is given by

$$\partial_z A_p = -\frac{1}{2}\alpha_p A_p + i\gamma_e \left(\sum_{p=1}^N 2|A_p|^2 - |A_p|^2 + 2|A_s|^2 \right) A_p, \quad (17)$$

and can be transferred to that at the incident signal as

$$\partial_z A_s = -\frac{1}{2}\alpha_s A_s + i\gamma_e \left(\sum_{j=1}^N 2|A_p|^2 + |A_s|^2 \right) A_s. \quad (18)$$

The degenerate FWM, governed by $2\omega_p = \omega_s + \omega_p$, results in N idlers that follow

$$\partial_z A_i = -\frac{1}{2}\alpha_i A_i + i\gamma_e \left[\sum_{p=1}^N 2|A_p|^2 + 2|A_s|^2 \right] A_i + i\gamma_e A_p^2 A_s^* \exp[i(2\beta_p - \beta_s - \beta_i)z]. \quad (19)$$

The degenerate FWM, governed by $2\omega_s = \omega_p + \omega_j$, also results in N idlers that follow

$$\partial_z A_j = -\frac{1}{2}\alpha_j A_j + i\gamma_e \left[\sum_{p=1}^N 2|A_p|^2 + 2|A_s|^2 \right] A_j + i\gamma_e A_s^2 A_p^* \exp[i(2\beta_s - \beta_p - \beta_j)z]. \quad (20)$$

Moreover, the non-degenerate FWM governed by $\omega_p + \omega_q = \omega_s + \omega_k$, where p and q denote the subscripts of different incident pumps, results in $N(N-1)/2$ idlers that follow

$$\partial_z A_k = -\frac{1}{2}\alpha_k A_k + i\gamma_e \left[\sum_{p=1}^N 2|A_p|^2 + 2|A_s|^2 \right] A_k + i\gamma_e 2A_p A_q A_s^* \exp[i(\beta_p + \beta_q - \beta_s - \beta_k)z]. \quad (21)$$

Meanwhile, the non-degenerate FWM, governed by $\omega_p + \omega_s = \omega_q + \omega_m$, results in $N(N-1)$ idlers that follow

$$\partial_z A_m = -\frac{1}{2}\alpha_m A_m + i\gamma_e \left[\sum_{p=1}^N 2|A_p|^2 + 2|A_s|^2 \right] A_m + i\gamma_e 2A_p A_s A_q^* \exp[i(\beta_p + \beta_s - \beta_q - \beta_m)z]. \quad (22)$$

While the data packet at incident signal wavelength is not converted to other idler wavelengths, Eq. (17–22) constitute the full-vectorial model that characterizes the resulting wavelength multicasting configuration with the output wavelength amount of $(3N^2 - N + 2)/2$. Additionally, the general full-vectorial model is valid in other straight waveguides, by varying the loss coefficient, the complex nonlinear coefficient and noteworthy by using the effective mode area given by Eq. (12).

Discussion

We derive the full-vectorial nonlinear propagation equations of the multiple-pumped four-wave mixing processes in straight waveguides, which takes the conventional simple form but becomes more accurate and study the dual-pumped case for one-to-six wavelength multicasting. We compare the numerical simulations of the conversion efficiency for the resulting idlers to the experimental measurements in a silicon-on-insulator waveguide sample and achieve a good agreement, which to our best knowledge is the first explicit validation of the numerical models. We characterize the conversion efficiency versus signal wavelength, which does not only show the incident signal wavelength, which produces high conversion efficiency for all idlers, but also enables the numerical prediction for the cases using multiple incident signals. We finally demonstrate the potential of the full-vectorial model to enlighten the experimental designs such as deciding pump/signal wavelength and the waveguide designs such as group-velocity dispersion tailoring, which benefit the future works of broadband wavelength multicasting configurations.

Methods

The SOI waveguide sample. The investigated waveguide sample is fabricated through the standard SOI nano-fabrication processes, including e-beam lithography and inductively coupled plasma etching. The height and the width of the waveguide are 250 nm and 450 nm, respectively. A silica cladding is deposited by the plasma enhanced chemical vapour deposition with a thickness of 1 μm . The transmittance of the photonic crystal grating couplers centres at 1550 nm, with a 3 dB bandwidth of 29 nm. All concerned wavelengths have anomalous group-velocity dispersion, where the second-order derivation of the propagation constant with respect to the angular frequency, β_2 , is $-1.4 \text{ ps}^2/\text{m}$ at 1555 nm.

The model derivation and the numerical simulation. The key points of the full-vectorial model derivation are: introduce Eq. (3) to avoid the cross product calculation of electric and magnetic vectors; define Eq. (12) to ensure that the complex nonlinear coefficient of Eq. (10) takes the conventional form²⁵ meanwhile the effective mode area becomes more accurate; predict all four-wave mixing processes to obtain the nonlinearity induced polarization contributed by all frequency components in Eq. (6); keep the terms being time-independent in the time integration of Eq. (4) and omit the terms contributed by generated idlers to simplify the final nonlinear propagation equations.

For a given waveguide structure, the cross-sectional distribution of the full-vectorial electric/magnetic fields and the resulting effective refractive index can be numerically calculated via open-source MATLAB codes³⁸, from which we estimate the effective mode area and the propagation constant at all the concerned wavelengths, substitute them into Eq. (14–22) and calculate the propagation evolution of the field amplitude through the finite element method. Our MATLAB code for the conversion efficiency calculation can directly retrieve the field distribution and the effective refractive index from the open-source codes, so the wavelength-dependence and the full-vectorial property are well kept in our numerical simulations.

Data Availability Statement

The datasets generated and analyzed during the current study are available from the corresponding author on reasonable request.

References

- Hansryd, J., Andrekson, P. A., Westlund, M., Li, J. & Hedekvist, P.-O. Fiber-based optical parametric amplifiers and their applications. *IEEE J. Sel. Top. Quantum Electron.* **8**, 506–520 (2002).
- Inoue, K. & Toba, H. Wavelength conversion experiment using fiber four-wave mixing. *IEEE Photonics Technol. Lett.* **4**, 69–72 (1992).
- Wang, W., Rau, L. G. & Blumenthal, D. J. 160 gb/s variable length packet/10 gb/s-label all-optical label switching with wavelength conversion and unicast/multicast operation. *J. Lightwave Technology* **23**, 211 (2005).
- Yoo, S. J. B. Wavelength conversion technologies for wdm network applications. *J. Light. Technol.* **14**, 955–966 (1996).
- Dong, P., Chen, Y.-K., Duan, G.-H. & Neilson, D. T. Silicon photonic devices and integrated circuits. *Nanophotonics* **3**, 215–228 (2014).
- Turner, A. C. *et al.* Tailored anomalous group-velocity dispersion in silicon channel waveguides. *Opt. express* **14**, 4357–4362 (2006).
- Dimitropoulos, D., Raghunathan, V., Claps, R. & Jalali, B. Phase-matching and nonlinear optical processes in silicon waveguides. *Opt. express* **12**, 149–160 (2004).
- Foster, M. A. *et al.* Broad-band optical parametric gain on a silicon photonic chip. *Nat.* **441**, 960 (2006).
- Espinola, R. L., Dadap, J. I., Osgood, R. M., McNab, S. J. & Vlasov, Y. A. C-band wavelength conversion in silicon photonic wire waveguides. *Opt. express* **13**, 4341–4349 (2005).
- Gao, S., Tien, E.-K., Song, Q., Huang, Y. & Boyraz, O. Ultra-broadband one-to-two wavelength conversion using low-phase-mismatching four-wave mixing in silicon waveguides. *Opt. express* **18**, 11898–11903 (2010).
- Ding, Y., Xu, J., Ou, H. & Peucheret, C. Mode-selective wavelength conversion based on four-wave mixing in a multimode silicon waveguide. *Opt. express* **22**, 127–135 (2014).
- Adams, R. *et al.* Wavelength conversion of 28 gbaud 16-qam signals based on four-wave mixing in a silicon nanowire. *Opt. express* **22**, 4083–4090 (2014).
- Pu, M. *et al.* Polarization insensitive wavelength conversion in a dispersion-engineered silicon waveguide. *Opt. express* **20**, 16374–16380 (2012).
- Biberman, A. *et al.* Wavelength multicasting in silicon photonic nanowires. *Opt. express* **18**, 18047–18055 (2010).
- Pu, M. *et al.* One-to-six wdm multicasting of dpsk signals based on dual-pump four-wave mixing in a silicon waveguide. *Opt. express* **19**, 24448–24453 (2011).
- Zhu, P. *et al.* Recursive pump-adding scheme for optical superchannel multicasting based on fwm. *Opt. Commun.* **347**, 25–30 (2015).
- Yang, W., Yu, Y. & Zhang, X. Integrated nonlinear interferometer with wavelength multicasting functionality. *Opt. express* **24**, 18217–18228 (2016).
- Xie, Y., Gao, S. & He, S. All-optical wavelength conversion and multicasting for polarization-multiplexed signal using angled pumps in a silicon waveguide. *Opt. letters* **37**, 1898–1900 (2012).
- Wang, X., Huang, L., Yi, K., Feng, X. & Gao, S. All-optical wavelength conversion and five-channel multicasting for 20 gbit/s qpsk signals in a silicon waveguide. *Opt. letters* **39**, 6122–6125 (2014).
- Wang, X., Huang, L. & Gao, S. Low-power-penalty wavelength multicasting for 36 gbit/s 16-qam coherent optical signals in a silicon waveguide. *Opt. letters* **39**, 6907–6910 (2014).
- Zhang, Y. *et al.* Performance analysis of dual-pump optical parametric amplifiers in silicon waveguide. *Opt. Commun.* **283**, 3043–3048 (2010).
- Du, Y. *et al.* Controlling four-wave mixing and six-wave mixing in a multi-zeeman-sublevel atomic system with electromagnetically induced transparency. *Phys. Rev. A* **79** (2009).
- Zhang, Y. *et al.* Four-wave mixing dipole soliton in laser-induced atomic gratings. *Phys. Rev. Lett.* **106**, 093904 (2011).
- Li, C. *et al.* Controlled correlation and squeezing in pr 3+:Y 2 sio 5 to yield correlated light beams. *Phys. rev. applied* **7** (2017).
- Lin, Q., Zhang, J., Fauchet, P. M. & Agrawal, G. P. Ultrabroadband parametric generation and wavelength conversion in silicon waveguides. *Opt. express* **14**, 4786–4799 (2006).
- McKinstrie, C. J., Radic, S. & Chraplyvy, A. R. Parametric amplifiers driven by two pump waves. *IEEE J. Sel. Top. Quantum Electron.* **8**, 538–547 (2002).
- Shoae, M. A., Mohajerin-Ariaei, A., Vedadi, A. & Brès, C.-S. Wideband generation of pulses in dual-pump optical parametric amplifier: theory and experiment. *Opt. express* **22**, 4606–4619 (2014).
- Liu, L. *et al.* Suppression of inter-channel higher order four wave mixing in four-mode phase-sensitive parametric wavelength multicasting. *J. Light. Technol.* **33**, 2324–2331 (2015).
- Agrawal, G. P. *Nonlinear Fiber Optics*, 4 edn (Elsevier, 2006).
- Yariv, A. Coupled-mode theory for guided-wave optics. *IEEE J. Quantum Electron.* **9**, 919–933 (2003).
- Snyder, A. W. & Love, J. *Optical waveguide theory* (Springer Science & Business Media, 2012).
- Kolesik, M. & Moloney, J. Nonlinear optical pulse propagation simulation: From maxwell's to unidirectional equations. *Phys. Rev. E* **70**, 036604 (2004).
- Afshar, S. & Monro, T. A full vectorial model for pulse propagation in emerging waveguides with subwavelength structures part i: Kerr nonlinearity. *Opt. Express* **17**, 2298–2318 (2009).
- Guo, K. *et al.* Full-vectorial propagation model and modified effective mode area of four-wave mixing in straight waveguides. *Opt. letters* **42**, 3670–3673 (2017).
- Claps, R., Raghunathan, V., Dimitropoulos, D. & Jalali, B. Influence of nonlinear absorption on raman amplification in silicon waveguides. *Opt. express* **12**, 2774–2780 (2004).
- Dimitropoulos, D., Jhaveri, R., Claps, R., Woo, J. & Jalali, B. Lifetime of photogenerated carriers in silicon-on-insulator rib waveguides. *Appl. Phys. Lett.* **86**, 071115 (2005).
- Tsang, H. K. *et al.* Optical dispersion, two-photon absorption and self-phase modulation in silicon waveguides at 1.5 μm wavelength. *Appl. Phys. Lett.* **80**, 416–418 (2002).
- Fallahkhair, A. B., Li, K. S. & Murphy, T. E. Vector finite difference modesolver for anisotropic dielectric waveguides. *J. Light. Technol.* **26**, 1423–1431 (2008).
- Ding, Y., Ou, H. & Peucheret, C. Ultrahigh-efficiency apodized grating coupler using fully etched photonic crystals. *Opt. letters* **38**, 2732–2734 (2013).
- Giles, C. R. & Desurvire, E. Modeling erbium-doped fiber amplifiers. *J. Light. Technol.* **9**, 271–283 (1991).

Acknowledgements

This work is supported jointly by the Chinese Scholarship Council, the Natural Science Foundation of China (60907003, 61671455), the Foundation of NUDT (JC13-02-13), the Hunan Provincial Natural Science Foundation of China (13JJ3001), the Program for New Century Excellent Talents in University (NCET-12-0142) and the Danish National Research Foundation (DNRF123). The authors would like to thank Karsten Rottwitz, Søren M. M. Friis, Yunhong Ding, Hao Hu, Sen Zhang, Jesper B. Christensen and Erik N. Christensen for their useful suggestions and linguistic supports.

Author Contributions

K. Guo, J. Feng, M. Gao and X. Shi derived the theoretical model; K. Guo, X. Wang and J. Yang conceived the experiments; K. Guo, J. Li and H. Jing conducted the experiments; H. Ou conducted the fabrication of the SOI waveguide sample; All authors discussed the results and reviewed the manuscript.

Additional Information

Competing Interests: The authors declare no competing interests.

Publisher's note: Springer Nature remains neutral with regard to jurisdictional claims in published maps and institutional affiliations.



Open Access This article is licensed under a Creative Commons Attribution 4.0 International License, which permits use, sharing, adaptation, distribution and reproduction in any medium or format, as long as you give appropriate credit to the original author(s) and the source, provide a link to the Creative Commons license, and indicate if changes were made. The images or other third party material in this article are included in the article's Creative Commons license, unless indicated otherwise in a credit line to the material. If material is not included in the article's Creative Commons license and your intended use is not permitted by statutory regulation or exceeds the permitted use, you will need to obtain permission directly from the copyright holder. To view a copy of this license, visit <http://creativecommons.org/licenses/by/4.0/>.

© The Author(s) 2018